Geometry optimization and effect of gas propellant in an electron cyclotron resonance plasma thruster

IEPC-2017-378
Presented at the 35th International Electric Propulsion Conference
Georgia Institute of Technology • Atlanta, Georgia • USA
October 8 – 12, 2017

Théo Vialis[1], Julien Jarrige[2] and Denis Packan[3]
ONERA-The French Aerospace Lab, Palaiseau, 91120, France

Abstract: In this paper, a parametric analysis of the geometry of the ONERA ECR plasma thruster is performed through direct thrust measurements. The results shown here are obtained with different dimensions (lengths and diameters) of the inner and outer conductor of the plasma source. The performance indicators (Thrust, Specific impulse, total efficiency) are compared and analyzed when the thruster is fed with xenon. The best performances are obtained with the longest source (20mm) and the highest diameter of the inner conductor (2.3mm) with 12.5 % of total efficiency. The use of krypton as an alternative propellant gas is also investigated. Higher performances are obtained with xenon but the operating pressure in the vacuum tank has probably a strong effect for krypton.

Nomenclature

T	=	thrust
I_{sp}	=	specific impulse
η_T	=	total efficiency
$TTPR$	=	thrust to power ratio
γ	=	calibration coefficient of the balance
η_m	=	mass efficiency
η_d	=	divergence efficiency
η_e	=	energy efficiency
Q_m	=	mass-flow rate
P	=	absorbed power
P_r	=	vacuum tank pressure
I_{tot}	=	total exhaust current
E_i	=	mean ion energy
J_i	=	ion density current

I. Introduction

Emerging technologies such as electrodeless plasma thruster are more and more studied as alternative for the more mature technologies which are the Gridded Ion Thrusters (GIT) and the Hall Effect Thrusters (HET)[1]. The advantage of the electrodeless thrusters is the quasi-neutrality of the plasma that is expelled: there is no need for a neutralization cathode, which is one of the most fragile components in ion and hall thrusters. Moreover, it makes the thruster insensitive to impurities in the propellant. This leads to a potentially higher reliability, longer lifetime, and lower development and recurring costs. But the complexity of the underlying physics involved is so far limiting

[1] PhD student, Physics and instrumentation department, theo.vialis@onera.fr
[2] Research scientist, Physics and instrumentation department, julien.jarrige@onera.fr
[3] Research scientist, Physics and instrumentation department, denis.packan@onera.fr

the development of this technology. One of the main difficulties is to model with enough precision all the mechanisms occurring simultaneously in the thruster such as ionization and plasma acceleration.
Among all the different concepts of this electrodeless technology, the most famous are the very powerful VASIMR (*Variable specific impulse magnetoplasma rocket*) developed by Ad-Astra Rocket in USA[2] and the Helicon Plasma Thrusters (HPT) initially proposed by R.W.Boswell in the 70's [3]. The ECR (Electron Cyclotron Resonance) plasma thruster developed at ONERA is based on an initial idea proposed in the 60's by H.G Kosmahl[4] that exploit the idea that electron resonance could be an efficient way to couple a wave energy to a plasma.

In order to compare the different electric propulsion technologies each other, one can define the following standard performance indicators:

— Total Efficiency: $\eta_T = T/(2\ Q_m\ \ P)$

— Specific Impulse: $I_{SP} = T/(Q_m g)$, where $g = 9.81\ m/s^2$ is the gravity constant,

As the purpose is to improve the technology, diagnostics over the thruster performances have been developed and are used to measure these performance indicators of the thruster prototype. Most of the results presented here comes from direct thrust measurements obtained on the ONERA's thrust stand presented in section II and in detailed in [5]. The balance thrust measurements does not give detailed information on the plasma properties. That is why complementary measurements with electrostatic diagnostics (such as the Faraday probe[6]) are useful, for example to measure the total ion current I_{tot} and the Ion mean energy E_i. This complementary information can help to improve the understanding and to identify ionization and the losses mechanism.

Previous works [7] have shown that the thruster efficiency can be estimated at 16% with a thrust level of 1 mN[8]. The performances are very sensitive to the operation conditions: the mass-flow rate, the injected power and the magnetic field magnitude. It has also been shown[9] that the ratio of ion energy over electron temperature, E_i/T_e, is constant for a given magnetic field configuration. In certain conditions, a polytropic expansion law can be used to model electron cooling and ion acceleration in the magnetic nozzle. An analytical discharge model of a helicon source has also been adapted to the ECR thruster[10] in order to improve the understanding of the physics involved.
Last year, this technology has been selected for funding in a European framework program called H2020 where the project name is: MINOTOR.

The purpose of this study is to optimize the ECR thruster performances by changing the design of the prototype and to analyze how the thruster is affected by changing the propellant gas from xenon to krypton.
The second section describes the ECR thruster technology, the operating conditions and the diagnostics. Section III presents the results obtained with different inner conductor lengths and diameters (III.A) and with different plasma source length (III.B). Finally, section IV presents the results obtained with krypton gas and the effect of the tank pressure on the thruster performances.

II. Experimental setup

The results presented here are obtained with the ONERA's ECR (electron cyclotron resonance) plasma thruster. This thruster is tested in the ONERA's B61 facility which is a 4m long and 1m diameter vacuum chamber with a three stages (primary, turbo-molecular, cryogenic) pumping system. The typical chamber pressure is about 5.10^{-6} mbar while the thruster is operating at 0.1 mg/s mass-flow rate of xenon.

A. Electron cyclotron plasma thruster

The thruster consists of a 27.5 mm diameter semi-open coaxial plasma source (Figure 1) in which a propulsive gas is injected and microwave power is fed. The source is immersed in a magnetic field created either by a coil or a permanent magnet. In the regions where the cyclotron frequency matches the frequency of the injected microwaves (e.g. in the areas where the magnetic field is around 875 G for a microwave frequency of 2.45 GHz), the free electrons from the plasma are heated by the cyclotron resonance effect. Microwave power is efficiently absorbed, while the electron temperature is increased up to a few tens of eV, and ionizes the propellant gas. The energetic electrons are expelled at the open side of the cavity (exhaust) by two main processes: plasma expansion (driven by the electron pressure) and diamagnetic effects in the divergent magnetic field. The difference of velocity between ions and electrons creates an ambipolar electric field that accelerates the ions in the magnetic nozzle to produce a current free and quasi-neutral plasma beam. Finally, the electrons detach themselves from the magnetic field lines in the far field. Moreover, the thruster is electrically insulated from the ground to ensure the neutrality of the expelled plasma. This compact coaxial geometry concept is under a European[11] and US patent.

The prototype, ECR-PM-V1 (Figure 2), that is used in this paper has been designed with an annular permanent magnet in order to be adapted to direct thrust measurement on a thrust balance. All its structure is made in aluminum

alloy except the plasma source back plate which is made of boron nitride. This prototype is typically operated with microwave input powers in the range 20-60 W at 2.45 GHz, and with xenon mass-flow rates in the range 0.05-0.2 mg/s. The thrust range is 300µN to 1.2mN.

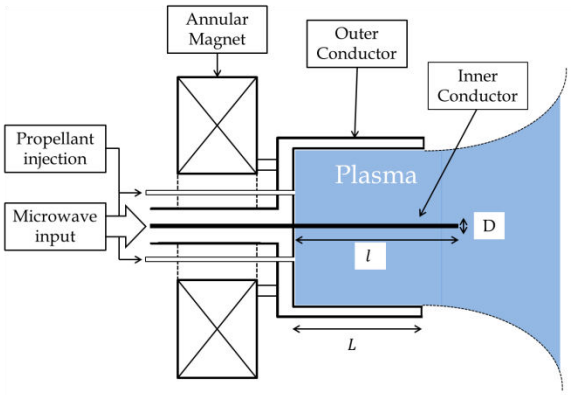

Figure 1. Schematic of the ECR-PM-V1 thruster

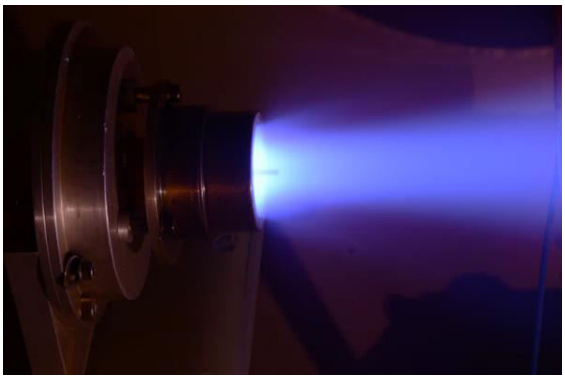

Figure 2. Picture of the ECR-PM-V1 thruster operating with xenon in the ONERA's B09 facility

A parametric study over the thrust geometry has been led, and the thruster performances are compared.

The current prototype design is modular. Different source configurations have been tested: three inner conductor lengths (15,20,25 mm), three inner conductor diameters (1.2,1.7,2.3 mm) and three outer conductor (plasma source) lengths (10,20,25 mm). The basic configuration of the thruster is: 20 mm long inner conductor, 1.7 mm inner conductor diameter and 15 mm long plasma source. The parameters are changed independently: for example when testing the 15 mm long inner conductor, the diameter is 1.7 mm and the plasma source is 15 mm long.

B. Thrust balance diagnostic

Direct thrust measurements are obtained by using a pendulum thrust balance (Figure 3) regulated by a PID control system. The PID maintains the arm of the balance at the equilibrium position. When the thruster is operated, the thrust is balanced by a force applied by an actuator (planar coil acting on magnets).

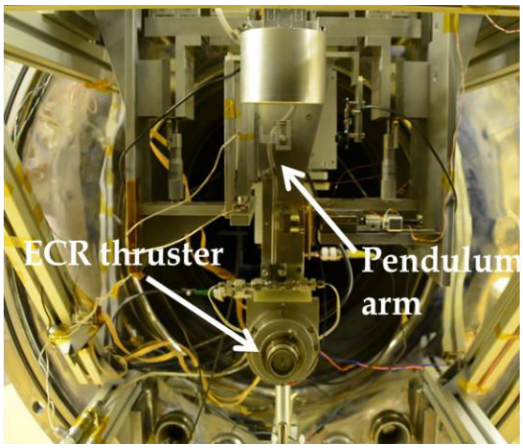

Figure 3. Picture of the ECR thruster mounted on the trust stand in the B61 vacuum chamber

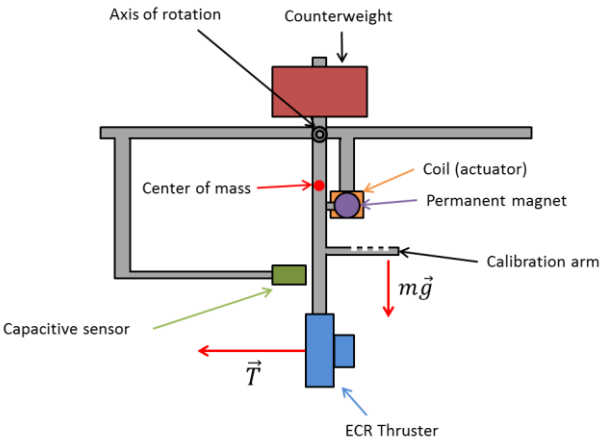

Figure 4. Schematic of the ONERA thrust balance

The displacement of the balance arm is measured with a capacitive sensor, while the current in the actuator is controlled by the PID control system. The current sent to the actuator is proportional to the thrust. The balance coefficient is obtained with an absolute calibration.

The calibration is performed by the deposition of small masses (m_i) with a known weight on the calibration arm (of length L_i) (Figure 4). The recorded signal is compared to the torque created by the masses in order to obtain the

calibration coefficient γ. A set of five calibrated masses are deposited in order to cover a thrust range from 100 µN to 1.5 mN. This method of calibration has very little uncertainty.

Figure 5 shows a typical example of a balance calibration. The coefficient γ is constant over the thrust range and the mean value is taken to convert the PID signal into thrust during thrust measurements.

A typical acquisition of the PID output signal during a thrust measurement of the ECR thruster is shown on Figure 6. The first peak corresponds to the thruster ignition. The operating conditions (mass-flow rate and power) are then adjusted, and the properties of the thruster are monitored during its stabilization.

Once the thruster has reached a steady-state regime (after ~1 minute) the power is turned off. The thrust value is obtained by measuring the step of PID voltage (V_{PID}) when the thruster is turned off. The absolute value of measured thrust is given by:

$$T = \frac{V_{PID}}{\gamma}$$

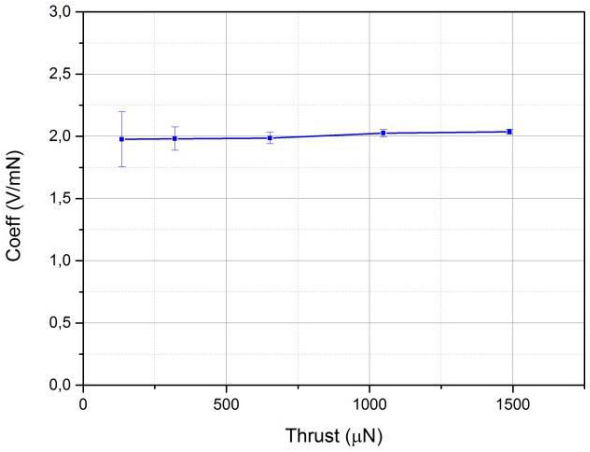

Figure 5. Example of calibration coefficient along the thrust range

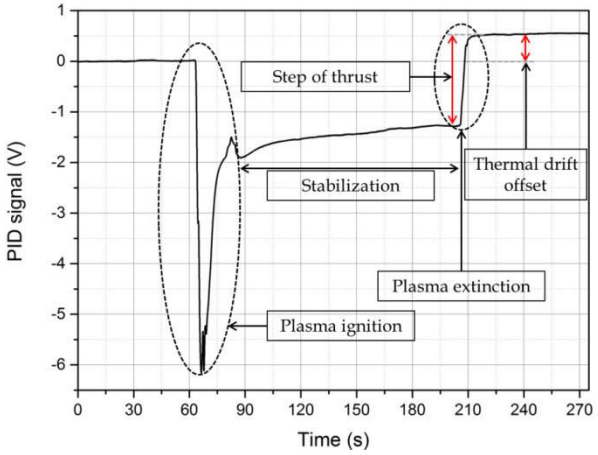

Figure 6. Typical thrust step signal with the different events during the acquisition

C. Faraday probe measurement

The thrust T can also be estimated from the angular profile of the ion current density J_i and from the mean ion velocity v_i in the axis. Both measurements are performed with a gridded Faraday probe mounted on a rotation stage. The expression of the thrust is:

$$T = \int_{-90}^{90} \frac{M_i}{e} J_i(\varphi\,) 2\pi D^2 v_i(\varphi) \sin(\varphi) \cos(\varphi)\, d\varphi$$

where m_i and e are respectively the ion mass and the elementary charge, D is the distance between the probe and the thruster. φ is the angle of rotation of the probe. Firstly, J_i is measured by negatively biasing the Faraday probe's collector at approximatively -300V in order to repel all electrons and to collect only the ions. An example of current

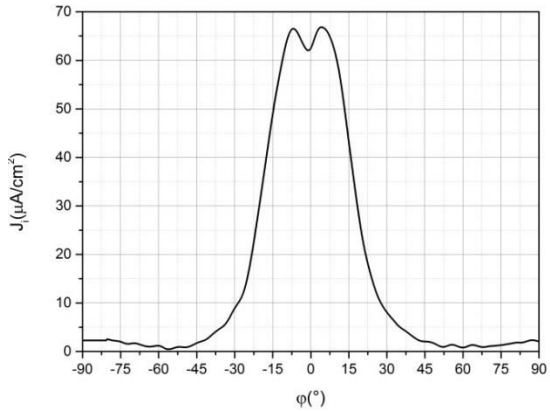

Figure 7. Typical angular profile of the ion current density

density angular profile is shown on Figure 7 (obtained with a 15 mm source length, 1.7 diameter and 20 mm long inner conductor). The total ion current is obtained by integrating the angular profile:

$$I_{tot} = \pi D^2 \int_{-90}^{90} J_i(\varphi) \sin(\varphi)\, d\varphi$$

Secondly, the ion velocity v_i is taken from: $v_i = \sqrt{2E_i/M_i}$ where M_i is the ion mass and E_i is the ion mean energy obtained by performing an energy scan with the Faraday probe. This technique is less accurate than standard electrostatic measurements of ion energy with 3-grids or 4-grids RPA that can give the ion energy distribution function, but sufficient to obtain the mean ion energy[12].

D. Typical results and error budget

The performance indicators (I_{sp}, η_T) can be deduced from the thrust measurement.

Figure 8 and Figure 9 present typical results from balance measurements with the measured thrust (Figure 8) and the deduced total efficiency (Figure 9) for four different mass-flow rates (0.06 mg/s to 0.125 mg/s) and three values of absorbed power (between 25 and 50 W). The experiments are performed with a 15 mm source length, 1.7 mm diameter and 20 mm long inner conductor. The results show the thrust increases with power and mass-flow rate from 500 µN for the lowest mass-flow rate and power to 950 µN for the highest mass-flow rate and power. Concerning the total efficiency, it is interesting to note that the slope sign changes depending on the mass-flow rate: for low Q_m (*i.e.* 0.06 & 0.08 mg/s) the efficiency decreases approximatively two points from 25 to 50 W. On the contrary, for higher Q_m (0.1 & 0.125 mg/s), the efficiency reaches a maximum value ($\eta_T \sim 8\%$) at the intermediate value of the power ($\sim 40W$). Finally for higher Q_m (not shown here), η_T decreases when increasing the power.

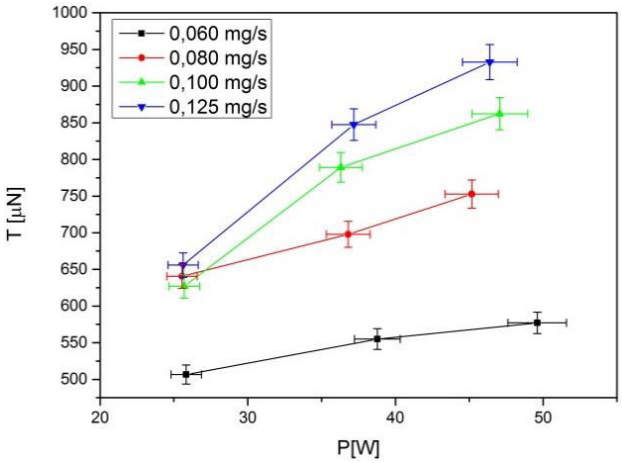

Figure 8. Measured thrust with respect to the injected power

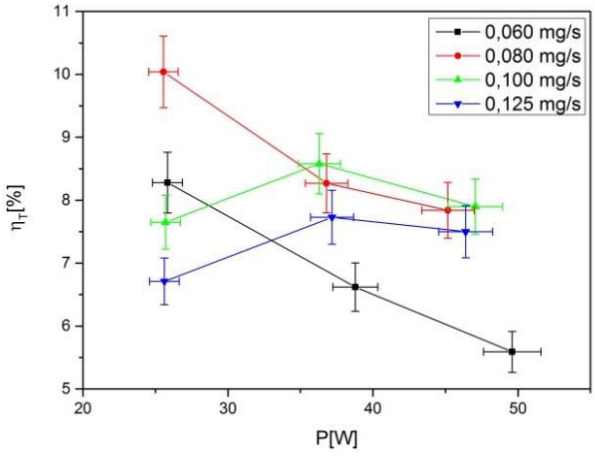

Figure 9. Measured total efficiency with respect to the

for four mass-flow rates **injected power for four mass-flow rates**

In order to compare the performances for the different conditions, another way to present the data is to plot the performance indicators as a function of the ratio of the mass-flow rate to absorbed power, Q_m/P. In particular, it is interesting to show the results in term of I_{SP} vs Q_m/P ratio (Figure 10) (see reference [5] for more details).

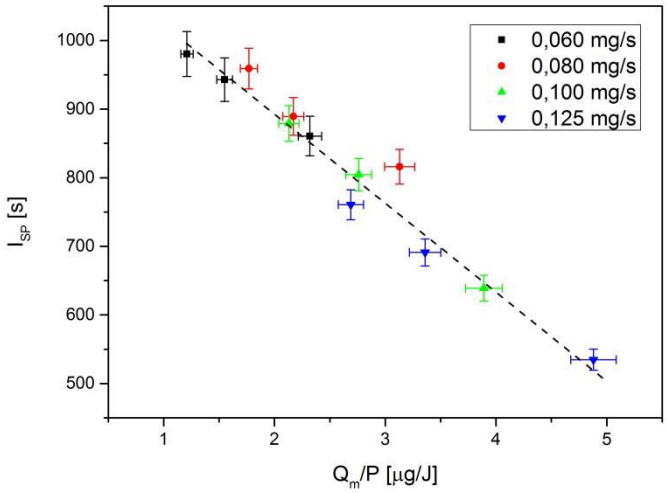

Figure 10. Specific impulse with respect to the Q_m/P ratio. The different colors represent the four mass-flow rates. A linear behavior is revealed in this range

In this case, for a given configuration (geometric, magnetic and propellant type), the I_{SP} decreases linearly with Q_m/P ratio in this range of power and flowrate. The I_{SP} drops from $1000\ s$ for the lowest Q_m/P ratio (1.2 µg/J) to $500\ s$ for the highest (5 µg/J). In the Figure 10 the different colors are the different Q_m. An important result is that, in this range, the I_{sp} only depends on the Q_m/P value: similar performances can be obtained for different mass flow rates as long as Q_m/P is kept constant.

This allows to simply comparing different thruster configurations on the same graph. For a given Q_m/P, the higher the I_{SP}, the higher the thruster efficiency.

Table 1 summarizes the different error sources taken in account in the error budget:

Table 1. Error budget for the direct thrust measurement

Quantity	Meaning	Uncertainty
V_{PID}	PID step signal	$20 \cdot 10^{-3}$ V
V_i	PID calibration signal	$30 \cdot 10^{-3}$ V
L_T	Balance arm length	$2 \cdot 10^{-3}$ m
L_i	Calibration arm length	$5 \cdot 10^{-4}$ m
m_i	Calibration mass	10^{-8} kg
g	Gravity constant	$< 10^{-4}$ m/s^2
Q_m	Mass-flow rate	$(0.01 + 0.005\ Q_m)$ mg/s
P	Microwave power	$(0.04\ P)$ W

The uncertainties over the thrust and the performance indicators are computed as following:

— Thrust: $\Delta T\ (mN) = \sqrt{\left(\frac{\Delta V_{PID}}{\gamma}\right)^2 + \left(\frac{\Delta V_i}{\gamma}\right)^2 + \left(\left(\frac{\Delta L_T}{L_T}\right)^2 + \left(\frac{\Delta L_i}{L_i}\right)^2\right) T^2}$

— Specific Impulse: $\Delta I_{SP} = I_{SP}\sqrt{\left(\frac{\Delta T}{T}\right)^2 + \left(\frac{\Delta Q_m}{Q_m}\right)^2}$

— Total efficiency: $\Delta \eta_T = \eta_T \sqrt{2\left(\frac{\Delta T}{T}\right)^2 + \left(\frac{\Delta Q_m}{Q_m}\right)^2 + \left(\frac{\Delta P}{P}\right)^2}$

These errors are represented as error bars on all the graphs in this paper. Note that, at this scale, the uncertainties over the calibration masses and over the gravity constant g can be neglected.

III. Geometry variations

A. Variation of the inner conductor geometry

The first results presented here are the variations of the geometry of the inner conductor. Figure 11 and Figure 12 shows pictures of the inner conductor used in the experiments for respectively three length l (Figure 11) and three diameters D (Figure 12).

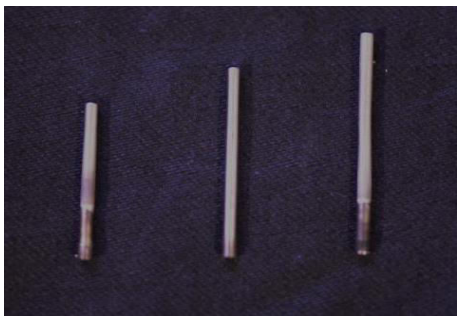

Figure 11. Picture of the three different length of inner conductor: 15, 20, 25 mm.

Figure 12. Picture of the three different diameter of inner conductor: 1.2, 1.7, 2.3 mm.

Firstly, Figure 13 presents the I_{SP} vs the Q_m/P ratio for the three inner conductor lengths. As shown in the last section, the I_{SP} decreases linearly with Q_m/P. In these three case: $l = 15, 20, 25$ mm, the I_{SP} goes from $\sim 1000\ s$ at $Q_m/P \sim 1.2\mu g/J$ to ~ 500 s at $Q_m/P \sim 5\ \mu g/J$. In this data set, the best efficiency is $\eta_T \sim 9\%$ at $Q_m/P \sim 2.8\mu g/J$. In this range, short inner conductors ($l = 15$ mm) produces slightly better results than the longer ones. However the increase of thruster performances is barely higher than the measurement uncertainty, so the effect of the inner conductor length is not significant between 15 and 25 mm.

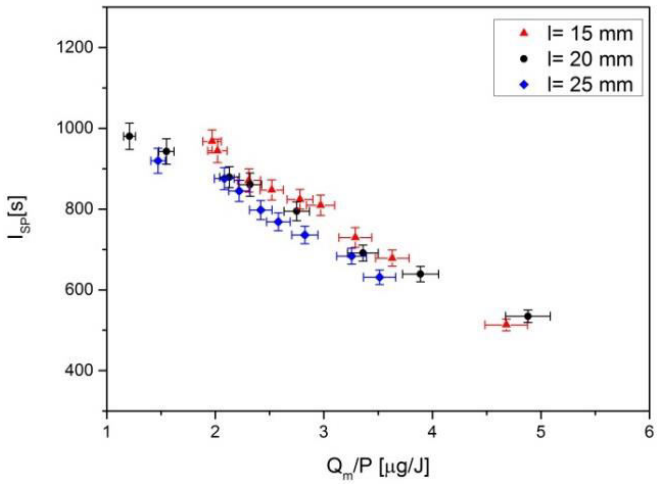

Figure 13. I_{SP} vs Q_m/P for the three different inner conductor lengths. Inner conductor diameter =1.7mm, outer conductor length =15 mm

Figure 14 now shows results obtained by varying the diameter of the inner conductor. This variation has a significant effect on the I_{SP} and therefore on the thruster performances. According to these results, higher diameters inner conductor makes the thruster more efficient. In the best case, which is $D = 2.3$ mm, the I_{SP} goes from ~500 s to $\sim 1100\ s$. In this case the maximum thruster efficiency is found to be close to 10%. In the meantime, the thinnest inner conductor gives lower performances with I_{SP} going from 800s to 400s with a maximum efficiency of $\sim 5.5\%$.

Note that the performance improvement due to the increase of the inner conductor diameter is particularly obvious for $Q_m/P < 2\mu g/J$. No significant differences are visible at $Q_m/P > 3\ \mu g/J$ between $D = 1.7$ mm and $D = 2.3$ mm.

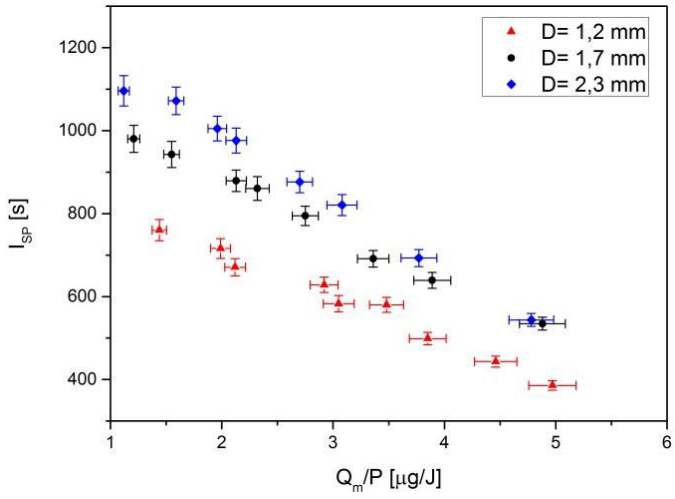

Figure 14. I_{SP} vs Q_m/P for the three different inner conductor diameters. Inner conductor length = 20 mm, outer conductor length = 15 mm

B. Variation of the outer conductor geometry

The effect of the in the plasma source length is now studied. The three sizes, L =10, 15, 20 mm, of the plasma source design are shown in Figure 15. The I_{SP} results are presented on Figure 16.

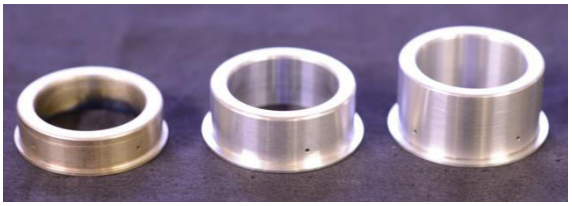

Figure 15. Picture of the three different length of plasma source: 10, 15, 20 mm.

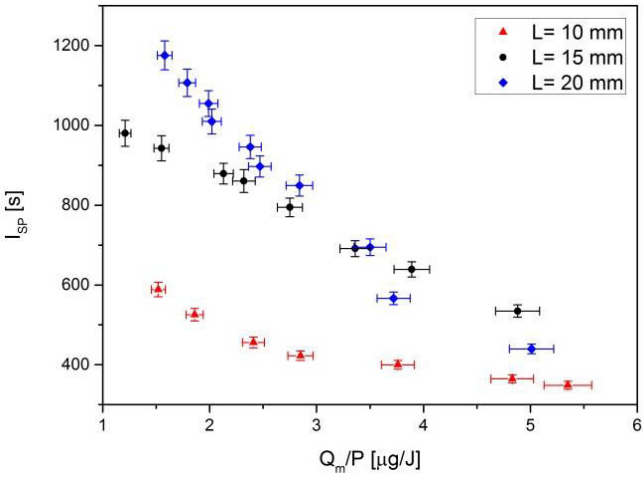

Figure 16. I_{SP} with respect to Q_m/P for the three different plasma source lengths. Inner conductor diameter = 1.7 mm, inner conductor length =20 mm

Significant differences are observed in this experiment. The performances seem to be increased by lengthening the plasma source. In the $L = 20$ mm case, the I_{SP} goes from ~1200 s to ~ 400 s. The maximum efficiency in this case is about 11%. On the other hand, with the shortest plasma source, the I_{SP} is in the range 300 - 600 s with a maximum efficiency of 3%.

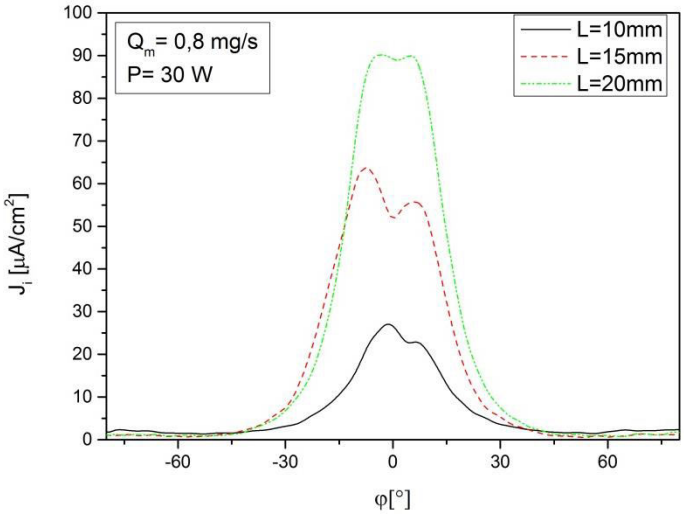

Figure 17. Angular scan of the ion current density J_i for the three different plasma source lengths. It has been performed with xenon at $Q_m = 0.08\ mg/s$ and $P = 30\ W$

In the meantime, data from Faraday probe measurement have shown that in the long source case, more ions are produced (Figure 17), *i.e.* total ion current I_{tot} is higher, than in shorter plasma source cases. However in the long source case, the expelled ions have a lower energy E_i. This observation could be explained by a higher mean density of neutral gas in the long source case compared to the short one. For a same power, an increase of high density neutral gas volume means more ionizing collisions and then, higher plasma density. The decrease of ion energy could be explained by a lower electron energy that could also due to the higher collision rate. Note that the divergence of the plasma beam is higher for the short source.

IV. Krypton as an alternative propellant and influence of the chamber pressure

The experiments presented here are led with the optimized geometry configuration of the thruster, *i.e.* 2.3 mm diameter inner conductor and 20 mm long plasma source.

Xenon is the most used propellant gas in electric thruster technologies because it is heavy ($M_{Xe} = 131.3$ g/mol) and quite easy to ionize ($E_I = 12.13\ eV$), which leads to better performances compared to other gases. However, as xenon is present at very low rate in the air, it is very expensive. For this last reason, it is particularly interesting to look at alternative propellant such as krypton which is less expensive because it is present in higher rate in the air. However, krypton is lighter ($M_{Kr} = 83.8$ g/mol) and harder to ionize ($E_I = 13.99\ eV$) than xenon. Both have the advantage of being noble gas and then non-reactive. This avoids toxicity and corrosive issues.

Figure 18 presents the comparison between xenon and krypton in the ONERA B61 vacuum tank. Xenon presents

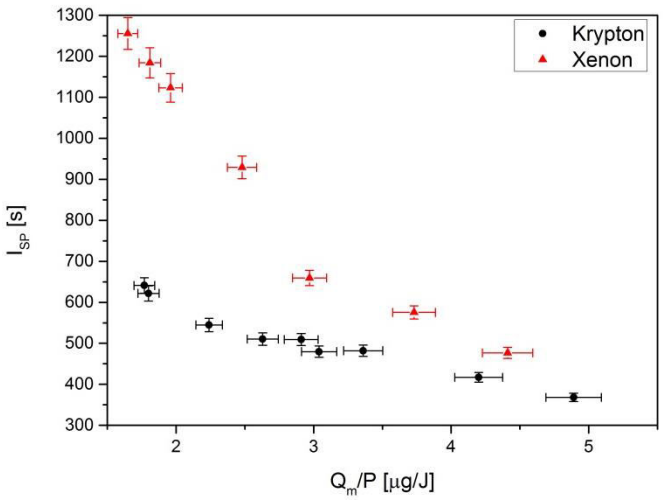

Figure 18. I_{SP} vs Q_m/P in comparison between xenon and krypton. The configuration is 20 mm plasma source and 2.3 mm diameter inner conductor

better performances than krypton: I_{SP} in the range 500- 1300 s for xenon in the range 350 - 650 s for krypton. The maximum efficiency in this configuration is 12.5% for xenon and 3.7% for krypton case.

Krypton being lighter than xenon is expected to have a higher I_{SP}, which is not the case here. This could be explained simply by the effect of the background pressure on the measured thrust. For the same flowrate (1.5 cm^3/s), the vacuum tank pressure is about $P_r \approx 6 \cdot 10^{-6}$ mbar and $P_r \approx 1.1 \cdot 10^{-5}$ mbar when the thruster is operated with xenon and krypton, respectively. This is due to the cryogenic pumping system of B61 vacuum chamber, which is a gas selective pumping. The pumping speed has been measured around 8000 l/s for the xenon but only around 3500 l/s for the krypton. Thus the effect of background pressure on measured performances was done.

V. Effect of background pressure on thruster performances.

While the ECR thruster is operated at a given condition (0.1 mg/s of xenon and 40W), the background pressure is varied by injecting a controlled mass flowrate of xenon directly in the vacuum chamber, at the opposite end of the chamber (thus no gas is directly impacting the thrust balance).

Results are shown in Figure 19 and Figure 20.

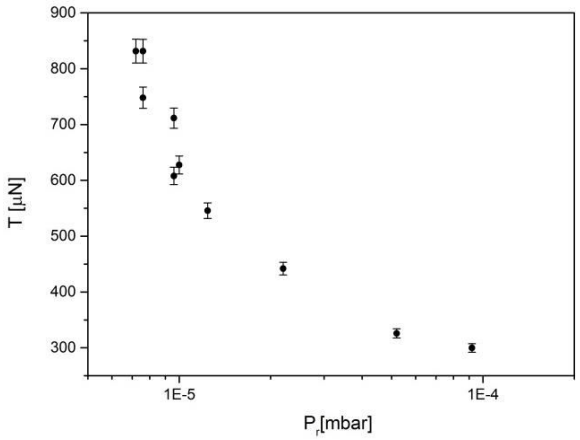

Figure 19. Thrust with respect to the background tank pressure

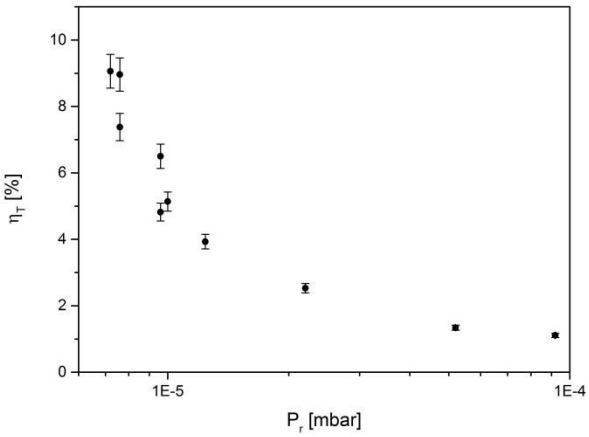

Figure 20. Total efficiency with respect to the background tank pressure

The measured thrust drops by a factor 1.5 when the background pressure is doubled. Without any added gas, the background pressure is $7.2 \cdot 10^{-6}$ mbar while the efficiency is measured at 9 % (configuration $L = 15\,mm$ and

$D = 1.7\ mm$). With an additional xenon injection of 0.4 mg/s, the background pressure is increased to $1.3 \cdot 10^{-5}$ mbar while the efficiency drops to 3.9 %. In parallel, Faraday probe measurements show a drop in the ion energy and a higher divergence of the plasma beam when the background pressure is increased. The ion current density decreases in the axis while raising on the edges (see Figure 21). However, the measured total ion current is roughly the same.

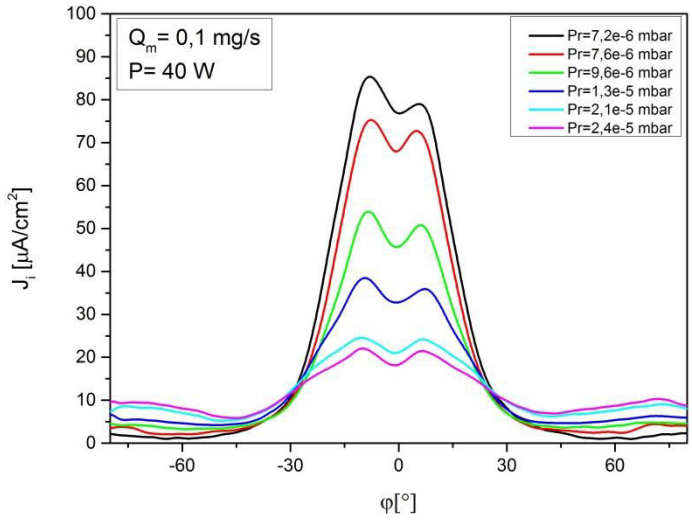

Figure 21. Angular scan of the ion current density J_i for six different background pressures. It has been performed with xenon at $Q_m = 0.1\ mg/s$ and $P = 40\ W$

It is remarkable that, contrary to hall thrusters, the ECR thruster performance drops dramatically as the pressure is increased. Several hypotheses could be made in order to explain this effect. One of them could be a high rate of charge exchange collisions leading to the dispersion of the plasma beam with low energy ions and high energy neutrals. However, with the actual background pressure the mean free path for the charge exchange collisions is several meters and the maximum loss rate is estimated[13] to be close to 3%. This could not explain totally the observed effect except if the pressure in the plume is at least one order of magnitude higher than the background one.

Another explanation could be that an ambient plasma is formed in the vacuum chamber because of the higher background pressure. This is consistent with the angular profiles of ion current density. This secondary plasma could disturb the plasma in the ECR source. This background plasma could also form a conductive layer around the thruster and plume, which would not be current free anymore. Further investigations are currently being performed.

VI. Conclusion

In this paper, an experimental geometry optimization of the ECR plasma thruster has been performed with a direct thrust measurement. It has been found that the inner conductor length does not play an important role in the thruster performances while the largest inner conductor diameter (2.3 mm) and the longest plasma source (20 mm) give the best results at low mass-flow rate over power ratio (Q_m/P). The maximum efficiency has been measured at ~12.5% (at 0.08mg/s and 50W) with this thruster configuration, corresponding to a thrust of ~ 1mN and 1250s of I_{SP}.The thruster has also been tested with krypton as propellant gas. A significant decrease of the performances has been observed with an efficiency not higher than 3.7% (at 0.1mg/s and 40W) corresponding to a thrust of ~ 550µN and 480s of I_{SP}. However, it has also been shown that the thruster performances are very sensitive to the background pressure, and a high pumping rate is needed in the vacuum chamber to obtain the best performances. The comparison of the results obtained with the two propellant gases needs to be done with the same conditions.

To go further, current investigations are conducted on the influence of the nature (conducting or insulating) of the source walls. Adapted geometry ($e.g.$ conical outer conductor parallel to the magnetic field lines) will be tested to reduce the losses on the walls. Higher power (typically 100 W) prototype of the thruster will also be tested.

Acknowledgments

This work was made in the framework of project MINOTOR that has received funding from the European Union's Horizon 2020 research and innovation program under grant agreement No 730028.

References

[1] Mazouffre S., "Electric propulsion for satellites and spacecraft : established technologies and novel approaches", Plasma Sources Sci. Technol., 25, 033002, 2016

[2] Longmier B.W. et al., "VX-200 Magnetoplasma Thruster performance results exceeding fifty-percent Thruster efficiency", Technical Notes in Journal Propulsion Power, Vol.27, No. 4, July-August, 2011

[3] R.W. Boswell, "Very Efficient Plasma Generation By Whistler Waves Near The Lower Hybrid Frequency", Plasma Phys. and Controlled Fusion, Vol.26, No10, pp. 1147 to 1162, 1984

[4] Kosmahl H.G. et al., "Plasma Acceleration with Microwaves near Cyclotron Resonance", J. Appl. Phys., Vol. 38, No. 12, November, 1967

[5] Vialis T., Jarrige J., Packan D., Aanesland A, "Direct thrust measurement of an electron cyclotron resonance plasma thruster", submitted to Phys. Plasmas, 2017

[6] Jarrige J. et Elias P-Q., Cannat F. and Packan D., "Characterization of a coaxial ECR plasma thruster", AIAA, Paper No. 2013-2628, 2013

[7] Cannat F. et al., "Experimental geometry investigation of a coaxial ECR plasma thruster", IEPC-2015-242/ISTS-2015-b-242

[8] Cannat F., Lafleur T., Jarrige J., Chabert P., Elias P-Q. and Packan D., "Optimization of a coaxial electron cyclotron resonance plasma thruster with an analytical model", Phys. Plasmas, Vol.22, 053503, 2015

[9] Lafleur T., Cannat F., Jarrige J., Elias P-Q. and Packan D., "Electron dynamics and ion acceleration in expanding-plasma thrusters", Plasma Sources Sci. Technol., Vol.24, 065013, 2015

[10] Lafleur T., "Helicon plasma thruster discharge model", Phys. Plasmas, Vol.21, 043507, 2014

[11] ONERA, INPI Brevet d'Invention, n11 62545, 2014

[12] Lafleur T., "Electrostatic Probe Diagnostics for Electric Propulsion Systems", Von Karman Institute conference, AVT 263-VKI, Belgium, 2016

[13] Scott Miller J. et al., "Xenon charge exchange cross sections for electrostatic thrusters models", J.App.Phys., 91, 984,2002